Int J Adv Manuf Technol (2000) 16:441–449

The International Journal of
Advanced
Manufacturing
Technology

Workspace Analysis of a Six-Degrees of Freedom, Three-Prismatic-Prismatic-Spheric-Revolute Parallel Manipulator

M. Z. A. Majid, Z. Huang and Y. L. Yao

Department of Mechanical Engineering, Columbia University, New York, USA

This paper studies the workspace of a six-degrees-of-freedom parallel manipulator of the general three-PPSR (prismatic-prismatic-spheric-revolute) type. It is known that a drawback of parallel manipulators is their limited workspace. To develop parallel mechanisms with a larger workspace is of use to potential applications. The mechanism of a three-PPSR manipulator and its variations are briefly analysed. The workspace is then investigated and the effects of joint limit and limb interference on the workspace shape and size are numerically studied. The constituent regions of the workspace corresponding to different classes of manipulator poses are discussed. It is shown that the workspace of this parallel manipulator is larger than that of a comparable Stewart platform, especially in the vertical direction.

Keywords: Parallel manipulator; Stewart platform; Workspace

1. Introduction

In the past decade, many researchers have shown an interest in parallel manipulators. Compared with the more commonly used serial manipulators, the parallel ones have advantages in accuracy, rigidity, capacity, and load-to-weight ratio. A parallel manipulator consists of a moving platform, a base platform and several branches connecting both platforms through appropriate kinematic joints with appropriate actuators. The best known parallel manipulator is the Stewart platform [1], which has been widely studied. In a Stewart platform, six bars connecting moving and base platforms are extensible to control the position and orientation of the moving platform.

Many different 6-degrees-of-freedom (DOF) parallel manipulators have been proposed. Recently, Tahmasebi and Tsai [2–5] introduced and studied a novel parallel manipulator (Fig. 1). This mechanism consists of an upper and a lower platform and three inextensible limbs. The lower end of each limb connects through a ball-and-socket joint to an actuator. The actuator is of a linear stepper type but is capable of moving in both *x*- and *y*-directions simultaneously on the base platform. The upper end of each limb is connected to the moving platform by a revolute joint. The manipulator is therefore a 3PPSR mechanism, where P denotes the prismatic pair, S the spherical pair, and R the revolute pair. The output motion of the 2D linear stepper motors is similar to that of two cross-prismatic pairs on the base platform. The desired motion of the upper platform is obtained by moving the actuators on the base platform, to which the lower ends of the three limbs are attached. Besides the merits of general parallel mechanisms over their serial counterparts mentioned before, this 3PPSR mechanism has added advantages, including simpler structure and higher stiffness. It is also less likely that its limbs will

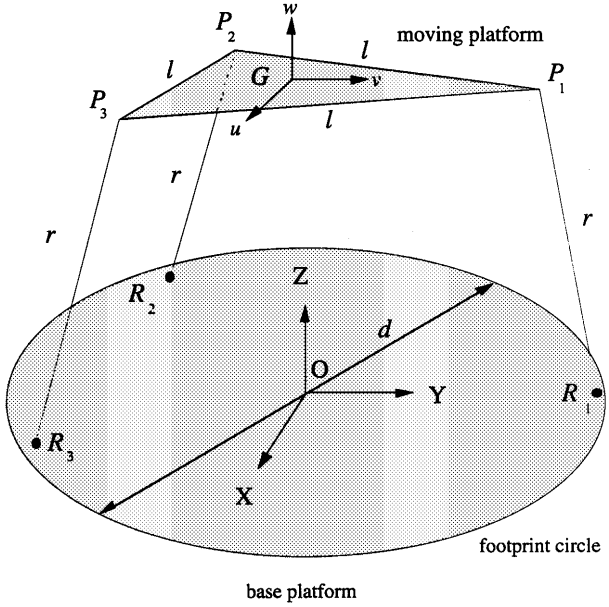

Fig. 1. A 3-PPSR parallel manipulator.

Correspondence and offprint requests to: Dr Y. Lawrence Yao, Department of Mechanical Engineering, Columbia University, 220 Mudd, MC 4703, New York, NY 10027, USA. E-mail: yly1@columbia.edu

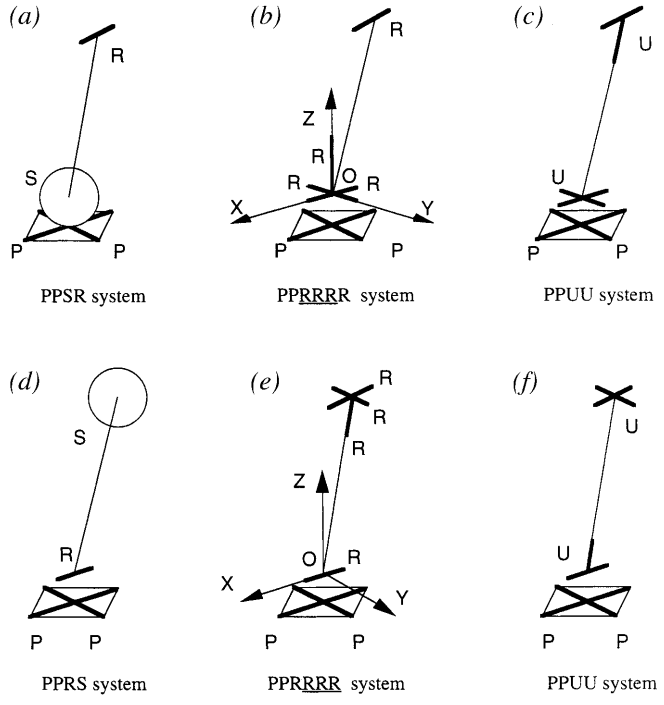

Fig. 2. Variations in pair sequence and type. (*a*), (*b*), and (*c*) form a kinematically equivalent set, whereas (*d*), (*e*), and (*f*) form another.

interfere with each other, since it has only three inextensible limbs instead of six extensible limbs as in a Stewart platform.

Tahmasebi and Tsai perceived this mechanism as being used as a minimanipulator, which can be mounted between the wrist and the end-effector of a serial manipulator for error compensation as well as for delicate position and force control. Therefore, the required workspace is rather small so that the motion of each actuator is limited to within a small circular area on the base platform when its workspace is considered [6]. The actuators carrying the limbs, however, do not have to be so restricted, they can move over the entire base platform, resulting in a much larger workspace. As a result, this 3PPSR mechanism can be used as a stand-alone manipulator. In addition, its special assembly of kinematic pairs makes it possible to have a workspace that is very different from and larger than that of a comparable Stewart platform. The study of workspace of a manipulator is one of the fundamental problems in the design of robot arms. As many researchers have pointed out, the major drawback of parallel mechanisms is their limited workspace. This 3PPSR parallel mechanism can help overcome the limitations of traditional parallel manipulators and extend the applications of parallel mechanisms. This paper analyses the size, shape, composition, and constraints of the workspace of the 3PPSR parallel manipulator.

The workspace of parallel manipulators has attracted the attention of many researchers over the past decade. Much reported work on parallel mechanism workspace dealt with 2DOF or 3DOF planar and spherical manipulators. Asada and Ro [7] and Bajpai and Roth [8] analysed the workspace of a closed-loop planar 2DOF 5-bar parallel mechanism. Gosselin and Angeles [9,10] studied the workspace of planar and spherical 3DOF mechanisms. Lee and Shah [11] and Waldron et al. [12] demonstrated the workspace of a spatial 3DOF in-parallel manipulator.

Much less work has been reported for the workspace of 6DOF parallel manipulators. Yang and Lee [13], Fichter [14], and Merlet [15] described the workspace of 6DOF parallel manipulators, using a method based on discretisation of the Cartesian space. Gosselin [16] used geometric properties to introduce an algorithm for determining the workspace of a 6DOF Stewart platform. His results showed that the workspace was the intersection of six annular regions. Masory and Wang [17] more systematically studied the workspace of a 6DOF Stewart platform. Their report discussed several constraint conditions for calculating its workspace, including the region of the angle of rotation of kinematic pairs and the interference between any two limbs of the mechanism. In addition, they analysed the shape of the workspace and the relationship between the workspace and the geometric parameters of the mechanism. Tahmasebi and Tsai [6] studied the workspace of this new 3PPSR parallel manipulator, where the motion of each of the three actuators attached to the lower end of each limb is limited to a small circular area. In the workspace analysis presented in this paper, limb interference and joint limitations are considered, and the actuators are allowed to move within a larger circle of diameter d (Fig. 1). The composition of the workspace is also studied by identifying the constituent regions according to different classes of manipulator poses.

2. Mechanism Analysis

As mentioned before, the upper and lower platforms of a 3PPSR mechanism are connected by three identical limbs each with the following kinematic pairs: double prismatic pairs, one spherical pair and one revolute pair (Fig. 2(*a*)). A spherical joint is kinematically equivalent to three non-coplanar revolute joints with a common point denoted as *RRR*. Thus the PP*RRR*R system shown in Fig. 2(*b*) is kinematically equivalent to the PPSR system. The PPSR arrangement is also kinematically equivalent to the limb shown in Fig. 2(*c*). This limb has a 2DOF universal joint at each of its lower and upper ends, where one of the axes of the upper universal joint is collinear with the limb, whereas another axis of the upper universal joint as well as one of the axes of the lower universal joint are always perpendicular to the limb [6]. In summary, the three structures: PPSR, PP*RRR*R, and PPUU, as shown in Figs 2(*a*), 2(*b*) and 2(*c*), are kinematically equivalent, where *U* denotes the universal joint. A similar structure, PPRS (Fig. 2(*d*)), can be obtained by exchanging the spherical pair and the revolute pair of the PPSR system. It is, however, kinematically different from the PPSR system, as shown below; but the PPRS system is kinematically equivalent to the two systems shown in Figs 2(*e*) and 2(*f*). Therefore, the set shown in Figs 2(*a*), 2(*b*), and 2(*c*) look similar but different from the set shown in Figs 2(*d*), 2(*e*) and 2(*f*).

Screw theory [18,19] is used in determining the difference between the two sets of structures. Every axis of the revolute joints can be expressed as a screw with zero pitch. The

PP*RRR*R system (Fig. 2(*b*)), which belongs to the first set, and PPR*RRR* (Fig. 2(*e*)), which belongs to the second set are taken as an example. A reference frame *oxyz* is defined for both PP*RRR*R and PPR*RRR*. The origin *o* is located at the intersecting point of two lines corresponding to the two directions of the 2D actuators. The *x* and *y*-axes lie collinear with the moving directions of the two prismatic pairs. The *z*-axis is defined by the right-hand-rule perpendicular to the base platform. Assuming that the limb is not collinear with the *z*-axis, two sets of screw systems may be given as follows:

Screw system 1 (for PP*RRR*R)	Screw system 2 (for PPR*RRR*)
$\$_{P11}$: (0 0 0; 1 0 0)	$\$_{P21}$: (0 0 0; 1 0 0)
$\$_{P12}$: (0 0 0; 0 1 0)	$\$_{P22}$: (0 0 0; 0 1 0)
$\$_{R13}$: (1 0 0; 0 0 0)	$\$_{R23}$: (1 0 0; 0 0 0)
$\$_{R14}$: (0 1 0; 0 0 0)	$\$_{R24}$: (0 1 1; 0 0 0)
$\$_{R15}$: (0 0 1; 0 0 0)	$\$_{R25}$: (0 1 0; −1 0 0)
$\$_{R16}$: (1 0 0; 0 1 1)	$\$_{R26}$: (1 0 0; 0 1 1)

From these two screw systems one can see that the six screws of each screw system are linearly independent, since their Jacobian matrices do not vanish

$$\det J_i = det[\$_{Pi1}\ \$_{Pi2}\ \$_{Ri3} \cdots \$_{Ri6}] \neq 0 \quad (i = 1, 2) \tag{2}$$

Here, one can see why one of the axes of the upper (lower) universal joint must be collinear with the limb, as shown in Figs 2(*c*) (2(*f*)). If this condition is not satisfied, the Jacobian matrix will become singular. For instance, if $\$_{R15}$ is not collinear with the limb (Fig. 2(*c*)) but is parallel with the *y*-axis, its screw becomes $\$_{R15}$ = (0 1 0; −1 0 0). The new Jacobian matrix involving $\$'_{R15}$ instead of $\$_{R15}$ in the screw system 1 will be singular owing to linear dependence. It is easy to see that $\$'_{R15}$ is a linear combination of $\$_{P11}$ and $\$_{R14}$. If all three legs of the parallel mechanism do not satisfy this condition, it will lose at least two degrees of freedom.

Note that, if the axis of the last revolute pair, $\$_{R16}$, of system PP*RRR*R (or PPSR) intersects the *Z*-axis, the last component of $\$_{R16}$ will be zero. That is, $\$_{R16}$: (*a b c*; *d e* 0), where *a*, *b*, *c*, *d*, and *e* are any real numbers, and the first three components (*a*, *b*, and *c*) and/or the last two (*d* and *e*) cannot all be zero. There exists a screw $\$^r$: (0 0 1; 0 0 0) which is reciprocal to all the six screws in screw system 1. This means that screw system 1 is linearly dependent, and only equivalent to a five-system screw [19]. The system loses one degree of freedom, that is, the translation along the *z*-axis. The entire 3PPSR mechanism will be singular, even if only one of its three limbs is in this condition. On the other hand, this type of singularity cannot exist for the screw system 2 (PPR*RRR* or PPRS), since the last three non-coplanar revolute pairs are equivalent to a spherical pair. Only two of the three axes can intersect the *Z*-axis simultaneously, and the third axis of the spherical pair cannot intersect the *Z*-axis at all.

Although they are linearly independent and both have six degrees of freedom, these two screw systems are different from each other. As a result, parallel mechanisms consisting of those different screw systems are also different, as illustrated in Fig. 3. The two mechanisms have the same geometrical parameters including leg lengths and moving triangles, the only difference being that one uses branches PPSR, and the other PPRS. Assuming that the upper and lower platforms are parallel initially, let the two upper platforms rotate from their initial positions for the same amount about B_2, B_4 and b_2, b_4, respectively. It is easy to see that the resultant positions of the two mechanisms are different.

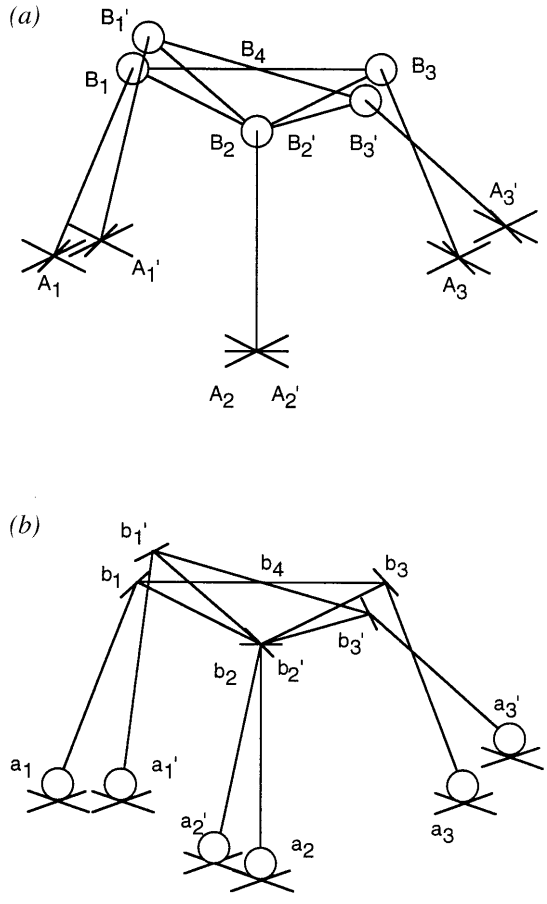

Fig. 3. Difference resultant displacements due to different structures. (*a*) A 3-PPRS mechanism. (*b*) A 3-PPSR mechanism.

3. Workspace Analysis

A fixed reference frame *OXYZ* is attached to the base platform, as shown in Fig. 1. The origin *O* is located at the centroid of the large circle with diameter *d*. The *X*- and *Y*-axes lie on the same base platform and the *Z*-axis is upward perpendicular to the base. The moving reference frame *Guvw* is attached to the moving platform. The point *G* is located at the centroid of the equilateral triangle. The *u*-axis is parallel with P_2P_3, and the *v*-axis passes through point P_1. The *w*-axis is perpendicular to the moving plane.

To determine the workspace of a mechanism, its direct kinematics is normally needed. Inverse kinematics, however, has always been applied for this purpose when parallel mechanisms are concerned, although inverse kinematics requires the use of a numerical solution. Given a pose (position and orientation) of the manipulator, the reference point of the upper platform determines an allowable point within the workspace, if the inverse kinematics of the given pose exists under all the

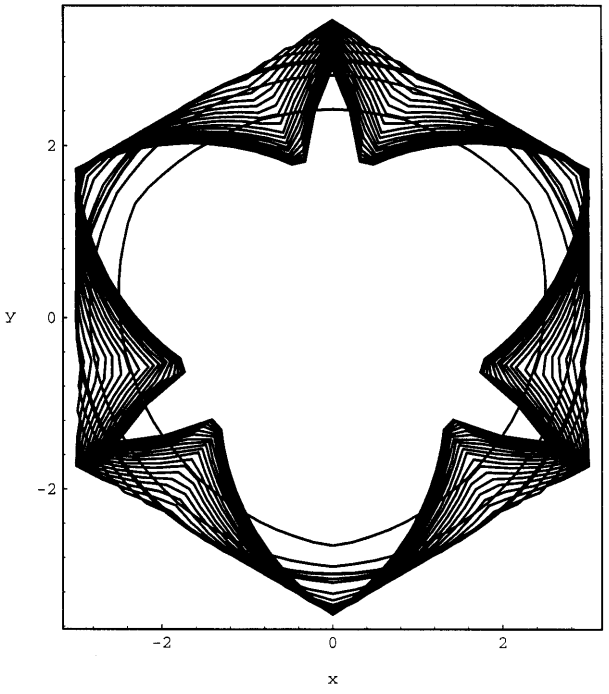

Fig. 4. Top view of workspace (case 1 : $\{\theta_u, \theta_v, \theta_w\} = \{0°, 0°, 0°\}$).

kinematic constraints. By giving a series of poses and obtaining a series of allowable points of the upper platform, the workspace becomes as an assembly of all the allowable points.

3.1 Inverse Kinematics

The coordinates of point P_i in the moving platform can be calculated via coordinate transformation when the pose of the upper platform is known. The orientation of the moving platform is given by Euler's angles yaw (θ_u), pitch (θ_v), and roll (θ_w). The coordinates of the centre point G with respect to the fixed frame are X_g, Y_g, and Z_g. The coordinate transformation matrix is

$$YPR(\theta_u, \theta_v, \theta_w) = \begin{bmatrix} \cos\theta_v \cos\theta_w & \sin\theta_u \sin\theta_v \cos\theta_w - \cos\theta_u \sin\theta_w & \cos\theta_u \sin\theta_v \cos\theta_w + \sin\theta_u \sin\theta_w & x_g \\ \cos\theta_v \sin\theta_w & \sin\theta_u \sin\theta_v \sin\theta_w + \cos\theta_u \cos\theta_w & \cos\theta_u \sin\theta_v \sin\theta_w - \sin\theta_u \cos\theta_w & y_g \\ -\sin\theta_w & \sin\theta_v \sin\theta_w & \cos\theta_u \cos\theta_v & z_g \\ 0 & 0 & 0 & 1 \end{bmatrix} \quad (3)$$

The coordinates of points P_1, P_2, and P_3 with respect to frame $Guvw$ are

$$P'_1 = (0, m, 0)^T$$
$$P'_2 = (-\tfrac{1}{2}, -\tfrac{1}{2} \tan 30°, 0)^T$$
$$P'_3 = (\tfrac{1}{2}, -\tfrac{1}{2} \tan 30°, 0)^T \quad (4)$$

where $m = \frac{1}{2} \cos 30°$. The coordinates of point P_i with respect to the fixed frame are

$$P_i = YPR(\theta_u, \theta_v, \theta_w) \begin{pmatrix} P'_i \\ 1 \end{pmatrix} \quad (i = 1, 2, 3) \quad (5)$$

From the geometry of the manipulator shown in Fig. 1, two simultaneous equations can be obtained. The first equation is:

$$(x_{p,i} - x_{r,i})^2 + (y_{p,i} - y_{r,i})^2 + (z_{p,i} - k)^2 = r^2 \quad (6)$$

where constant k is the Z-coordinate of point R_i. The subscripts p, i and r, i denote points P_i and R_i, respectively. This is the equation for a circle on the base. The second equation follows from the perpendicularity of vector $\mathbf{R}_i\mathbf{P}_i$ and vector $\mathbf{P}_{i+1}\mathbf{P}_{i+2}$. Since the joint at point P_i is revolute, point R_i is the intersection of the circle of Eq. (6) with the plane that contains vector $\mathbf{R}_i\mathbf{P}_i$ and is normal to vector $\mathbf{P}_{i+1}\mathbf{P}_{i+2}$. That is,

$$\mathbf{P}_{i+1}\mathbf{P}_{i+2} = \langle n_x, n_y, n_z \rangle = \langle x_{p,i+2} - x_{p,i+1}, y_{p,i+2} - y_{p,i+1}, z_{p,i+2} - z_{p,i+1} \rangle \quad (7)$$

The equation of the plane is given as

$$n_x(x_{p,i} - x_{r,i}) + n_y(y_{p,i} - y_{r,i}) + n_z(z_{p,i} - k) = 0 \quad (8)$$

Equations (6) and (8) are solved for $x_{r,i}$ and $y_{r,i}$,

$$\begin{aligned} x_{r,i} = [&-kn_x^2n_z + n_x^3x_{p,i} + n_xn_y^2x_{p,i} + n_x^2n_zz_{p,i} \mp n_xn_y(-k^2n_x^2 \\ &- k^2n_y^2 - k^2n_z^2 + n_x^2r^2 + n_y^2r^2 + 2kn_x^2z_{p,i} \\ &+ 2kn^2yz_{p,i} + 2kn_z^2z_{p,i} - n_x^2z_{p,i}^2 - n_y^2z_{p,i}^2 - n_z^2z_{p,i}^2)^{0.5}]/[n_x^3 + n_xn_y^2] \\ y_{r,i} = [&-kn_y^2n_z + n_x^2y_{p,i} + n_y^2y_{p,i} + n_yn_zz_{p,i} \pm n_x(-k^2n_x^2 - k^2n_y^2 \\ &- k^2n_z^2 + n_x^2r^2 + n_y^2r^2 + 2kn_x^2z_{p,i} + 2kn_y^2z_{p,i} \\ &+ 2kn_z^2z_{p,i} - n_x^2z_{p,i}^2 - n_y^2z_{p,i}^2 \\ &- n_z^2z_{p,i}^2)^{0.5}]/[n_x^3 + n_xn_y^2] \end{aligned} \quad (9)$$

Because Eq. (6) is a second-order polynomial, $x_{r,i}$ and $y_{r,i}$ can have two values. These two values are valid as long as they satisfy the joint limit and interference conditions, and are within the allowable footprint space.

3.2 Kinematic Constraints

In determining the workspace of a 3PPSR manipulator, three types of kinematic constraints are considered. They are the diameter of the footprint circle, joint angle limits, and link interference.

Footprint Circle. The positions of the lower ends of all three limbs must be inside the footprint circle (Fig. 1), that is

$$|\mathbf{R}_i| \leq d/2 \quad (10)$$

where d is the diameter of the footprint circle and $\mathbf{R}_i$ denotes the radius vector of point R_i with respect to the origin O.

Joint Angle Constraints. The links are attached to the upper and lower plates by kinematic pairs which have physical limits. For instance, a ball joint is theoretically free to rotate 360° about each of the three orthogonal axes. In practice, however, its motion is restricted by the physical construction of the joint within a relatively small range. Thus, there is a need to impose a maximum rotational angle θ_{max} for each joint. The rotational angle and its limitation can be expressed as

$$\theta_i = \cos^{-1}((\mathbf{v}_i \cdot \mathbf{u}_i)/|\mathbf{v}_i|) \leq \theta_{i,max} \quad (11)$$

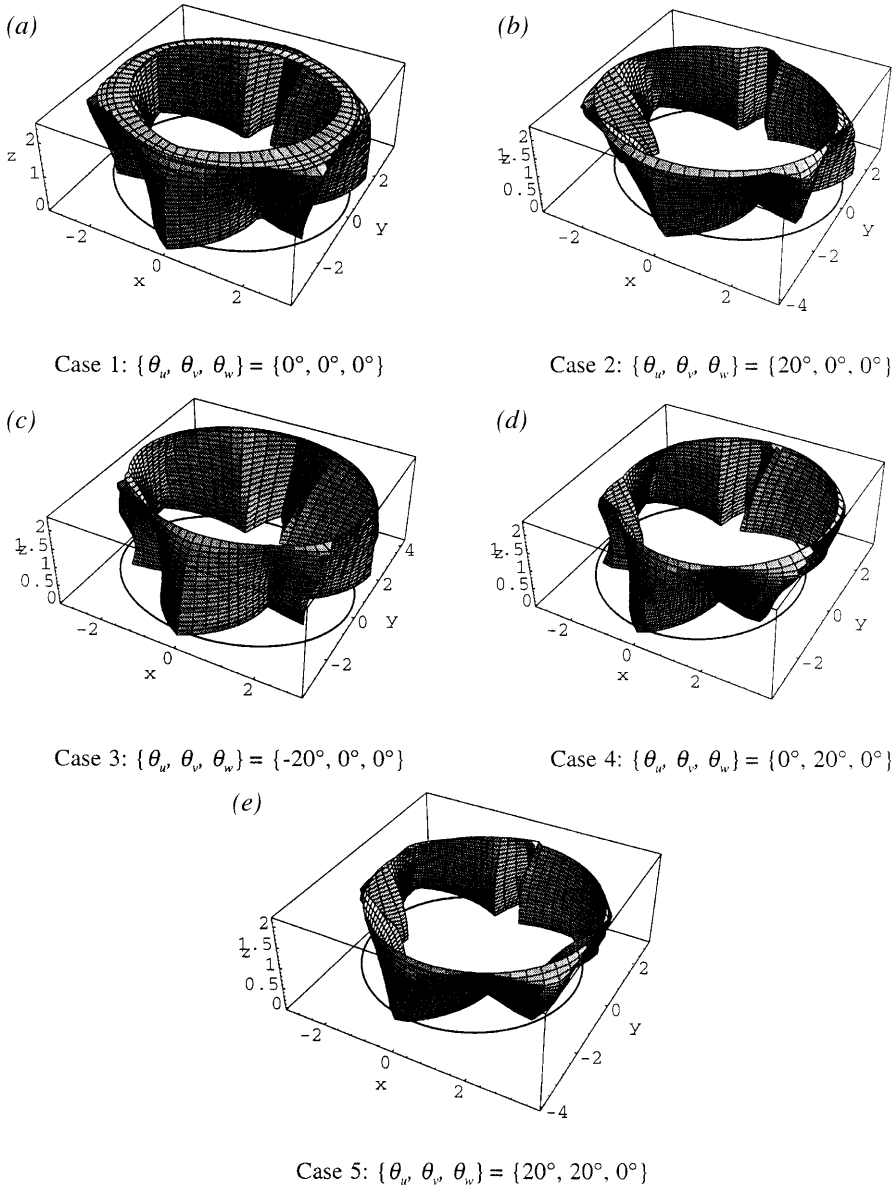

Fig. 5. Theoretical workspace boundary (without joint limit and interference constraints) (without showing the top and bottom plates of the boundary for viewing convenience).

where $\mathbf{v}_i$ is the vector of link l_i, and $\mathbf{u}_i$ is a vector representing the line which bisects the rotational range of each kinematic pair with respect to the fixed frame.

Link Interference. Since links have physical dimensions, interference might occur. Assume that each link is cylindrical with a diameter d_1, and D is the shortest distance between two adjacent links l_i and l_{i+1}, the interference limitation can be expressed by

$$d_1 \leq D \tag{12}$$

The shortest distance between the centre-lines of two links is the length D_n of their common normal $\mathbf{n}_i$. That is

$$D_n = |\mathbf{n}_i \cdot \mathbf{P}_i\mathbf{P}_{i+1}| \tag{13}$$

where the unit vector $\mathbf{n}_i$ of the common normal direction between two adjacent links l_i and l_{i+1} can be obtained as

$$\mathbf{n}_i = (\mathbf{v}_i \times \mathbf{v}_{i+1})/|\mathbf{v}_i \times \mathbf{y}_{i+1}| \tag{14}$$

Note that, the shortest distance between links is not always equal to the length D_n of the common normal. It could be larger than D_n. The shortest distance from point P_i to the link l_{i+1}, if the intersection point C_i of the link l_i and the common normal of the two links is situated beyond the link l_i itself, or the intersection point M_i of the link l_i and the perpendicular line from point P_i+1 to link l_i is situated beyond link l_i itself. The shortest distance is the distance between the two endpoints P_i and P_{i+1}, if the two intersection points, M_i and M_{i+1}, are both beyond links l_i and l_{i+1} [17].

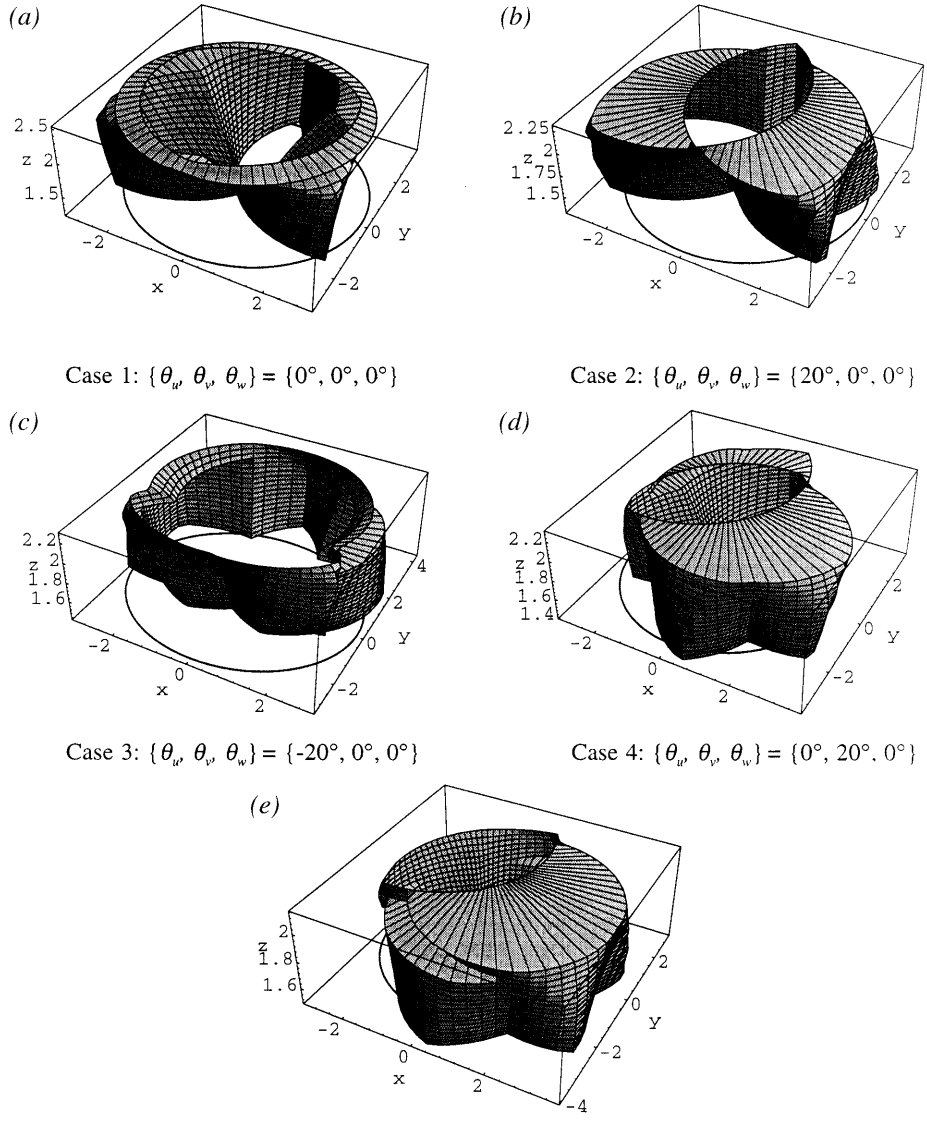

Fig. 6. Practical workspace boundary (with joint limit and interference constraints) (without showing the top and bottom plates of the boundary for viewing convenience).

Three lines, including two adjacent links and their common normal, define two planes. The normals of these two planes are

$$\frac{\mathbf{n}_i \times \mathbf{v}_i}{|\mathbf{n}_i \times \mathbf{v}_i|} = \langle a_i, b_i, c_i \rangle$$

$$\frac{\mathbf{n}_i \times \mathbf{v}_{i+1}}{|\mathbf{n}_i \times \mathbf{v}_{i+1}|} = \langle a_{i+1}, b_{i+1}, c_{i+1} \rangle \tag{15}$$

The equations of the two planes are

$$a_i(x - x_{p,i}) + b_i(y - y_{p,i}) + c_i(z - z_{p,i}) = 0 \tag{16}$$

$$a_{i+1}(x - x_{p,i+1}) + b_{i+1}(y - y_{p,i+1}) + c_{i+1}(z - z_{p,i+1}) = 0 \tag{17}$$

A line in 3D space can be represented as

$$\frac{x - x_{p,i}}{v_{x,i}} = \frac{y - y_{p,i}}{v_{y,i}} = \frac{z - z_{p,i}}{v_{z,i}} \tag{18}$$

The equations of two centre-lines of two adjacent legs can be resolved from

$$v_{y,i}(x - x_{p,i}) - v_{x,i}(y - y_{p,i}) = 0 \tag{19}$$

$$v_{z,i}(y - y_{p,i}) - v_{y,i}(z - z_{p,i}) = 0 \tag{20}$$

$$v_{y,i+1}(x - x_{p,i+1}) - v_{x,i+1}(y - y_{p,i+1}) = 0 \tag{21}$$

$$v_{z,i+1}(y - y_{p,i+1}) - v_{y,i+1}(z - z_{p,i+1}) = 0 \tag{22}$$

where Eqs (19) and (20) represent the centre-line of link, l_i, and Eqs (21) and (22) the centre-line of link l_{i+1}.

The intersection point C_i between line l_i and the common normal is obtained by solving Eqs (17), (19) and (20), simultaneously.

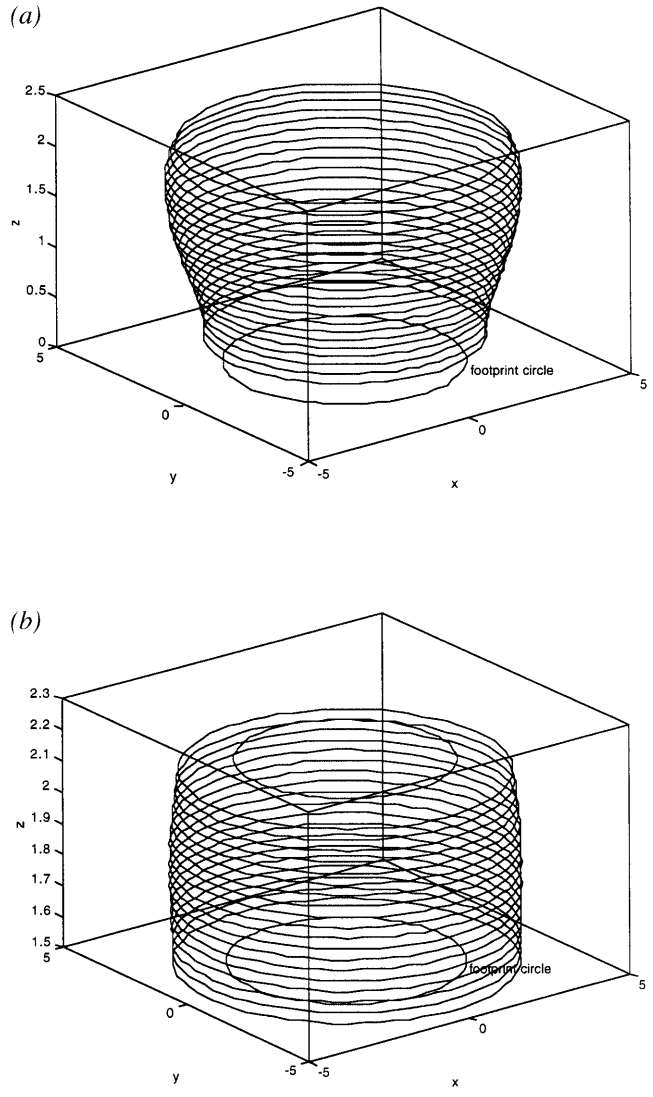

Fig. 7. Actual workspace obtained by revolving the boundaries shown in Figs. 5 and 6 about the *Z*-axis for 360°. (*a*) Theoretical (case 5, Fig. 5(*e*)). (*b*) Practical (case 5, Fig. 6(*e*)).

$$
\begin{aligned}
x_{\text{intercept},i} &= [a_i v_{x,i+1} x_{p,i} + b_i (v_{y,i+1} x_{p,i+1} + v_{x,i+1} y_{p,i} - v_{x,i+1} y_{p,i+1}) \\
&\quad + c_i (v_{z,i} x_{p,i+1} + v_{x,i+z_{p,i}} - v_{x,i+1} z_{p,i+1})]/[a_i v_{x,i+1} + b_i v_{y,i+1} + c_i v_{z,i}] \\
y_{\text{intercept},i} &= [a_i (v_{y,i+1} x_{p,i} - v_{y,i+1} x_{p,i+1} + v_{x,i+1} y_{p,i+1}) + b_i v_{y,i+1} y_{p,i} + c_i (v_{z,i} y_{p,i+1} \\
&\quad + v_{y,i+1} z_{p,i} - v_{y,i+1} z_{p,i})]/[a_i v_{x,i+1} + b_i v_{y,i+1} + c_i v_{z,i}] \\
z_{\text{intercept},i} &= [a_i (v_{z,i} x_{p,i} - v_{z,i} x_{p,i+1} + v_{x,i+1} z_{p,i+1}) + b_i (v_{z,i} y_{p,i} - v_{z,i} y_{p,i+1} \\
&\quad + v_{y,i+1} z_{p,i+1}) + c_i v_{z,i} z_{p,i}]/[a_i v_{x,i+1} + b_i v_{y,i+1} + c_i v_{z,i}]
\end{aligned}
\tag{23}
$$

Equations (16), (21), and (22) are solved simultaneously to obtain the intersection point C_{i+1} on line $i+1$.

$$
\begin{aligned}
x_{\text{intercept},i+1} &= [a_{i+1} v_{x,i} x_{p,i+1} + b_{i+1} (v_{y,i} x_{p,i+1} + v_{x,i} y_{p,i+1} - v_{x,i} y_{p,i}) \\
&\quad + c_{i+1} (v_{z,i+1} x_{p,i} + v_{x,i} z_{p,i+1} - v_{x,i} z_{p,i})]/[a_{i+1} v_{x,i} + b_{i+1} v_{y,i} + c_{i+1} v_{z,i+1}] \\
y_{\text{intercept},i+1} &= [a_{i+1} (v_{y,i} x_{p,i+1} - v_{y,i} x_{p,i} + v_{x,i} y_{p,i}) \\
&\quad + b_{i+1} v_{y,i} y_{p,i+1} + c_{i+1} (v_{z,i+1} y_{p,i} + v_{y,i} z_{p,i+1} - v_{y,i} z_{p,i+1})]/[a_{i+1} v_{x,i} \\
&\quad + b_{i+1} v_{y,i} + c_{i+1} v_{z,i+1}]
\end{aligned}
$$

$$
\begin{aligned}
z_{\text{intercept},i+1} &= [a_{i+1} (v_{z,i+1} x_{p,i+1} - v_{z,i+1} x_{p,i} + v_{x,i} z_{p,i}) \\
&\quad + b_{i+1} (v_{z,i+1} y_{p,i+1} - v_{z,i+1} y_{p,i} + v_{y,i} z_{p,i}) \\
&\quad + c_{i+1} v_{z,i+1} z_{p,i+1}]/[a_{i+1} v_{x,i} + b_{i+1} v_{y,i} + c_{i+1} v_{z,i+1}]
\end{aligned}
\tag{24}
$$

For the 3-PPSR mechanism considered in this paper, all six links are located between two plates. Interference is therefore impossible if $Z_{C_i} \geq Z_{P_i}$ and $Z_{C_{i+1}} \geq Z_{P_{i+1}}$.

4. Numerical Examples and Discussion

The workspace subject to the above-mentioned constraints is numerically studied. Each link is assumed to be cylindrical, and the geometric parameters are given as $r = 2.5$ units, $l = 1.0$ units, $d = 6$ units, $d_1 = 0.15$ units, $\theta_{r,\max} = 75°$, $\theta_{s,\max} = 60°$, and $k = 0$, where r denotes the leg length of P_iR_i, l the length of each side of the moving triangle, d the diameter of the footprint circle on the base platform, d_1 the diameter of the links. $\theta_{r,\max}$ and $\theta_{s,\max}$ are the allowable maximum angles of rotation for the revolute joint and the spherical joint, respectively, and constant k denotes the Z coordinate of point R_i.

The 3D workspace is presented in two graphical forms, i.e. a 2D top view, and a 3D isometric view of the workspace boundary, without showing the upper and lower portions of the boundary for viewing convenience. Since the workspace involves both position and orientation, it is 6D and therefore three invariable Euler angles are specified for each case below. In order to demonstrate the different situations and the effects of constraints on workspace size and shape, five typical cases are studied.

Case 1 : $\{\theta_u, \theta_v, \theta_w\} = \{0, 0, 0\}$
Case 2 : $\{\theta_u, \theta_v, \theta_w\} = \{20, 0, 0\}$
Case 3 : $\{\theta_u, \theta_v, \theta_w\} = \{-20, 0, 0\}$
Case 4 : $\{\theta_u, \theta_v, \theta_w\} = \{0, 20, 0\}$
Case 5 : $\{\theta_u, \theta_v, \theta_w\} = \{20, 20, 0\}$

Note that, since the platform is symmetric about the *v*-axis of the moving platform, the case of $\{\theta_u, \theta_v, \theta_w\} = \{0°, -20°, 0°\}$ will be the same as $\{\theta_u, \theta_v, \theta_w\} = \{0°, 20°, 0°\}$. In addition, θ_w remains zero in all five cases because the shape of the workspace will remain the same for any θ_w value. This is in turn because the workspace will simply rotate by θ_w for any non-zero θ_w value without shape change.

Figure 4 shows shows the top view of the workspace for case 1 where $\{\theta_u, \theta_v, \theta_w\} = \{0°, 0°, 0°\}$. Figure 5 includes isometric views of the theoretical workspace for all five cases where the effects of joint angle constraints and interference are not considered, while Fig. 6 shows isometric views of the practical workspace for the same five cases where all the kinematic constraints are considered. It is seen that the shapes and the structures of the workspaces of this 3-PPSR parallel mechanism are completely different from that of traditional parallel mechanisms. It allows a larger range of motion in the *Z*-direction especially.

It should be pointed out that the workspaces shown in Figs 5 and 6 are obtained when θ_w is kept at zero. Since θ_w can rotate by 360°, the actual shape of the workspace is obtained by rotating the shapes shown in Figs 5 and 6 about the *Z*-axis

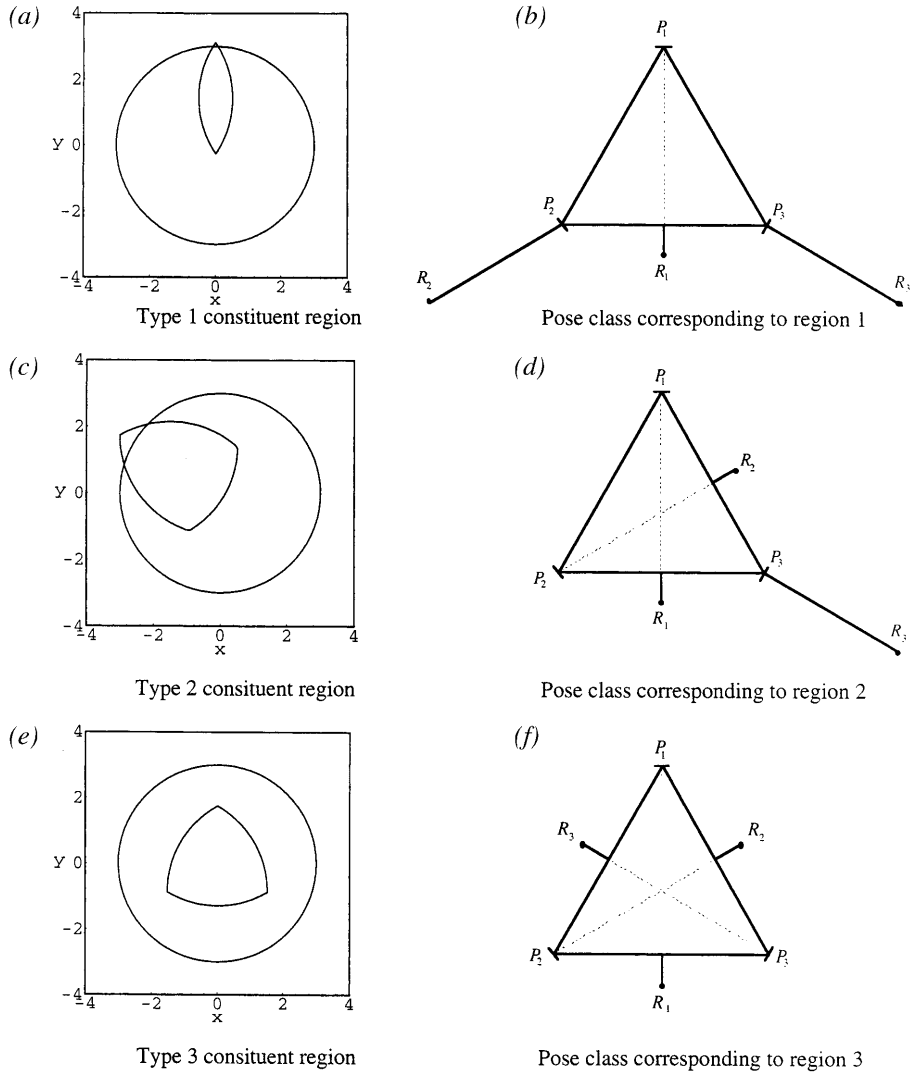

Fig. 8. Constituent regions and corresponding classes of poses case 1: $\{\theta_u, \theta_v, \theta_w\} = \{0°, 0°, 0°\}$ (the footprint circle of diameter 6 units is also shown in (*a*), (*c*), and (*e*)).

by 360° (Fig. 7). Compared with a comparable Stewart platform, which usually has a workspace in the shape of a mushroom cap, this workspace has a cylindrical shape and therefore a larger Z range.

The workspace is examined in detail to understand its composition. The examination is achieved through decomposing the workspace into its constituent regions according to different classes of manipulator poses. The workspace shown in Fig. 4 (case 1) is used as an example. Four types of constituent regions can be identified for, say, $Z = 1.0$.

Type 1 region: the shape (superposed on the footprint circle) in Fig. 8(*a*), which corresponds to the pose in which leg 1 points toward the platform and other two legs point outward from the platform (Fig. 8(*b*)). Alternatively, legs 2 or 3 may point toward the platform while leg 1 points outward, giving a region similar to, but 120° apart from, the region shown in Fig. 8(*a*).

Type 2 region: the shape (superposed on the footprint circle) in Fig. 8(*c*), which corresponds to the pose in which both legs 1 and 2 point toward the platform while the third points outward from the platform (Fig. 8(*d*)). Alternatively, legs 2 and 3 and 1 may point toward the platform while the third points outward, giving regions similar to, but again 120° apart from, the region shown in Fig. 8(*c*).

Type 3 region: the shape (superposed on the footprint circle) in Fig. 8(*e*), which corresponds to the pose in which all three legs point toward the platform (Fig. 8(*f*)).

Type 4 region: the shape similar to the one shown in Fig. 8(*e*), which corresponds to the pose in which all three legs point outward from the platform. This type of region has no practical effect on workspace determination since it is always a subset of the type 3 region.

All these regions are plotted in Fig. 9, where a footprint circle of diameter 6 units is also plotted. It is clear that the

intersection of these regions forms an area which is identical to that shown in Fig. 4. It is, therefore, clear that they are the constituent regions of the workspace.

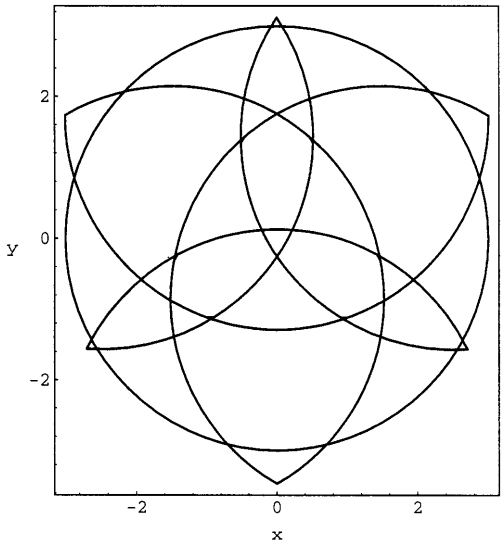

Fig. 9. Intersection of the constituent regions forms the workspace (case 1: $\{\theta_u, \theta_v, \theta_w\} = \{0°, 0°, 0°\}$) (the footprint circle of diameter 6 units is also shown).

5. Conclusion

In this paper, the workspace of the 3-PPSR manipulator is analysed. It is shown that the workspace consists of three types of region, each corresponding to a class of manipulator poses. The effects of kinematic constraints, including revolute and spherical joint limitations and limb interference on workspace structure are shown. The 3-PPSR manipulator has a workspace of cylindrical shape, while a Stewart platform usually has a mushroom-cap type of workspace, which allows limited motion in the *Z*-direction.

References

1. D. Stewart, "A platform with six degrees of freedom", Proceedings Institution of Mechanical Engineers, 180, pp. 25–28, 1965.
2. F. Tahmasebi and L.-W. Tsai, "On the stiffness of a novel six-DOF parallel manipulator", Intelligent Automation and Soft Computing, Proceedings of the First World Automation Congress (WAC'94), vol. 2, pp. 189–194, 1994.
3. F. Tahmasebi and L.-W. Tsai, "Closed-form direct kinematics solution of a new parallel manipulator", Journal of Mechanical Design, 116, pp. 1141–1147, 1994.
4. L.-W. Tsai and F. Tahmasebi, "Synthesis and analysis of a new class of six-DOF parallel manipulators", Journal of Robotic Systems, 10, pp. 561–580, 1993.
5. F. Tahmasebi and L.-W. Tsai, "Jacobian and stiffness analysis of a novel class of six-DOF parallel manipulators", Proceedings of the 22nd Biennial Mechanisms Conference, ASME, DE-vol. 47, pp. 95–102, 1992.
6. F. Tahmasebi and L.-W. Tsai, "Workspace and singularity analysis of a novel six-DOF parallel manipulator", Journal of Applied Mechanisms and Robotics, 1(2), pp. 31–40, 1994.
7. H. Asada and I. H. Ro, "A linkage design for direct drive robot arms", Journal of Mechanisms, Transmissions and Automation in Design, 107, pp. 536–540, 1985.
8. A. Bajpai and B. Roth, "Workspace and mobility of a closed-loop manipulator", International Journal of Robotics Research, 5(2), pp. 131–142, 1986.
9. C. Gosselin and J. Angeles, "The optimum kinematic design of a planar three-DOF parallel manipulator", Journal of Mechanisms, Transmissions and Automation in Design, 110, pp. 35–41, 1988.
10. C. Gosselin and J. Angeles, "The optimum kinematic design of a spherical three-DOF parallel manipulator", Journal of Mechanisms, Transmissions and Automation in Design, 111, pp. 202–207, 1989.
11. K. M. Lee and D. K. Shah, "Kinematic analysis of a three-DOF in-parallel actuated manipulator," IEEE Journal of Robotics and Automation 4(3), 354–360, 1988.
12. K. J. Waldron, M. Raghavan and B. Roth, "Kinematics of a hybrid series of parallel manipulation system", ASME Journal of Dynamic System Measurement and Control, 111, pp. 211–221, 1989.
13. D. C. H. Yang and T. W. Lee, "Feasibility study of a platform type of robotic manipulators from a kinematic viewpoint", Journal of Mechanisms, Transmissions and Automation in Design, 106, pp. 191–198, 1984.
14. E. F. Fichter, "A Stewart platform-based manipulator: general theory and practical construction", International Journal of Robotics Research, 5(2), pp. 157–182, 1986.
15. J. P. Merlet, "Force-feedback control of parallel manipulator", IEEE International Conference on Robotics and Automation, pp. 1484–1489, 1988.
16. C. Gosselin, "Determination of the workspace of six-DOF parallel manipulator", Journal of Mechanical Design, 112, pp. 331–336, 1990.
17. O. Masory and J. Wang, "Workspace evaluation of Stewart platform", Proceedings ASME Winter Annual Meeting, DE-45, pp. 337–352, 1992.
18. R. S. Ball, Theory of Screw, Cambridge University Press, 1900.
19. K. H. Hunt, Kinematic Geometry of Mechanisms, Oxford, Clarendon Press, 1978.